Optimization of the figure of merit in $Bi_{100-x}Sb_x/Al_2O_3$ nanocomposites

Hyungyu Jin[1,*] and Joseph P. Heremans[2]

[1]*Department of Mechanical Engineering, Pohang University of Science and Technology (POSTECH), Pohang 37673, South Korea*

[2]*Department of Mechanical and Aerospace Engineering, Department of Materials Science and Engineering, and Department of Physics, The Ohio State University, Columbus, Ohio 43210, USA*

(Received 17 May 2018; published 26 November 2018)

Bismuth-antimony ($Bi_{100-x}Sb_x$) alloys have the highest thermoelectric figure of merit of all *n*-type thermoelectric materials below 200 K. They are the only Te-free thermoelectric alternatives to the tetradymite materials for applications at and below room temperature. Single-crystal $Bi_{100-x}Sb_x$ alloys show the maximum figure of merit $zT \sim 0.5$ at 200 K along the trigonal axis crystallographic direction, but the cost associated with single-crystal growth and the tendency of single crystals to cleave preclude their use. Mechanically robust polycrystalline $Bi_{100-x}Sb_x/Al_2O_3$ nanocomposites are shown here to be able to reach competitive zT values. Two compositions are investigated, $Bi_{82}Sb_{18}$ and $Bi_{88}Sb_{12}$. Thermal and electrical transport properties confirm significant reduction of lattice thermal conductivity in the nanocomposite samples, but the concurrent loss of electrical conductivity leads to an unfavorable net effect on zT. In contrast, a large increase in thermopower is observed in the $Bi_{82}Sb_{18}/Al_2O_3$ nanocomposite system, which is attributed to a better optimized doping level. Accordingly, the zT of a $Bi_{82}Sb_{18}/Al_2O_3$ nanocomposite sample is shown to reach $zT \sim 0.4$ at 240 K, which rivals that of single crystals. Near room temperature, the zT of the nanocomposite sample is improved by ~60% over that of the single-crystalline sample. Galvano- and thermomagnetic analysis suggests a strong effect of carrier concentration on the zT of $Bi_{100-x}Sb_x/Al_2O_3$ nanocomposite samples.

DOI: 10.1103/PhysRevMaterials.2.115401

I. INTRODUCTION

Bismuth-antimony ($Bi_{100-x}Sb_x$) alloys have the highest zT of all *n*-type thermoelectric materials below about 200 K [1]. Unlike elemental Bi, which is a semimetal with a band overlap [2], $Bi_{100-x}Sb_x$ alloys with $7 < x < 20$ become narrow-gap semiconductors with a finite band gap whose size depends on x [3]. The semiconducting $Bi_{100-x}Sb_x$ alloys show better thermoelectric performance compared to elemental Bi, because in elemental Bi, electron and hole partial thermopowers compensate each other, which leads to an overall thermopower that is smaller than in semiconductors with the same charge carrier concentration. Alloy scattering of phonons also lowers the lattice thermal conductivity of $Bi_{100-x}Sb_x$ alloys compared to that of elemental Bi. Finally, unlike the commercial tetradymite $(Bi_{100-x}Sb_x)_2(Te_{100-y}Se_y)_3$ alloys [4] that dominate the thermoelectric industry, $Bi_{100-x}Sb_x$ alloys contain no Te, an element that is rare in the Earth's crust. In cost-sensitive thermoelectric applications, the Peltier elements sometimes are cut so small that the effective Peltier-module figure of merit or ZT (typically 0.4–0.7) is greatly reduced compared to the material zT (typically 0.9–1.2). Here, the material has a $zT \equiv (\frac{S^2\sigma}{\kappa})T$, where S is the Seebeck coefficient or thermopower, σ the electrical conductivity, κ the thermal conductivity, and T the temperature. Under those circumstances, using larger $Bi_{100-x}Sb_x$ elements at a lower material cost may be competitive with smaller $(Bi_{100-x}Sb_x)_2(Te_{100-y}Se_y)_3$ elements producing the same net device ZT. Unfortunately, values of $zT \geqslant 0.4$ until now have been achieved only in single-crystal $Bi_{100-x}Sb_x$ ($x < 20$ at.%) alloys along the trigonal axis direction normal to the cleavage plane, raising unsurmountable mechanical problems in Peltier coolers.

While extensive studies have been done on thermoelectric properties of single-crystalline $Bi_{100-x}Sb_x$ alloys [5–9] as well as polycrystalline samples [10–13], almost no noticeable improvement has been achieved in zT of these alloys, still limited to a maximum zT of ~0.5 at 200 K for single-crystalline samples. Due to strong anisotropy, single-crystalline $Bi_{100-x}Sb_x$ alloys possess much better thermoelectric performance along the trigonal axis direction, compared to that in the trigonal plane direction consisting of binary and bisectrix axes. The room temperature zT of single-crystalline $Bi_{100-x}Sb_x$ alloys for different x values as reported by Yim and Amith [5] is shown in Fig. 1. The zT is maximum around $x = 12$ at.% in both trigonal axis and binary/bisectrix axis (trigonal plane) directions, but the anisotropy decreases markedly above $x = 15$ at.%. These single-crystalline alloys cleave easily along the trigonal plane direction, which presents mechanical stability issues for practical applications, as mentioned above. Polycrystalline $Bi_{100-x}Sb_x$ alloys, on the other hand, comprise small crystals with random orientations, which make them more robust against mechanical stress and have thermoelectric performance somewhere between that of trigonal axis and trigonal plane directions. To estimate the zT of polycrystalline $Bi_{100-x}Sb_x$ alloys for different x values, Fig. 1 also shows the average of the single-crystal data, and the results show good agreement with the experimental results by Lenoir *et al.* [11]. The average has a broad maximum centered

*hgjin@postech.ac.kr

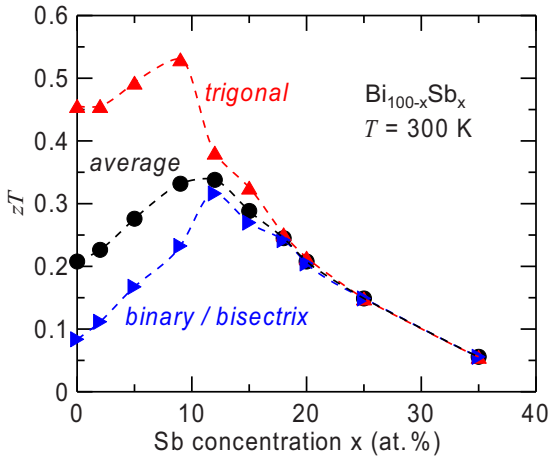

FIG. 1. Calculated thermoelectric figure of merit (zT) of $Bi_{100-x}Sb_x$ alloys at 300 K from the data on the undoped single-crystalline samples in Ref. [5]. The result for the polycrystal ("average") was obtained by taking weighted averages of the data along the three crystallographic directions. Symbols indicate calculated data points and lines are added to guide the eye.

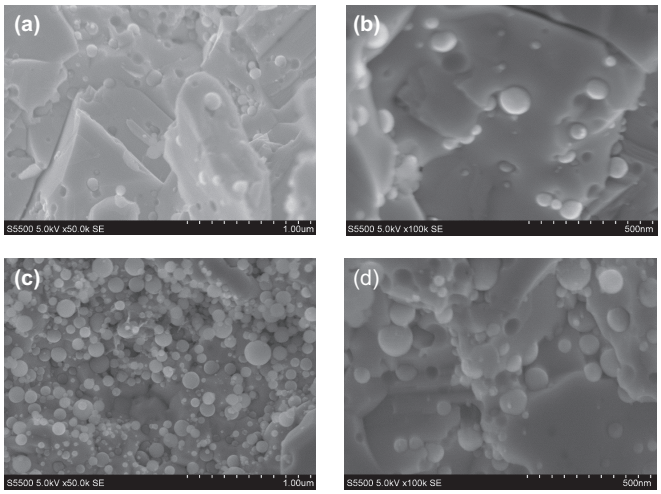

FIG. 2. Scanning electron microscopy (SEM) pictures for $Bi_{82}Sb_{18}/Al_2O_3$ nanocomposite samples with (a), (b) 5 vol % and (c), (d) 20 vol % Al_2O_3 nanoparticles. Scale bar is shown on the bottom-right corner of each picture.

around $x = 12$ at.%; the present study therefore is focused on this concentration and also on $x = 18$ at.% for comparison.

It has been shown [14–17] that under circumstances where the electron mean free path is much shorter than the phonon mean free path, nanostructuring can effectively reduce the lattice thermal conductivity of thermoelectric materials while not affecting S and σ that much, thus leading to improvement of zT. Although proven effective, nanostructuring has fundamental limitations in practical applications due to grain growth during thermal cycles at temperatures near the melting point. Besides the thermal conductivity reduction, nanostructuring was also suggested as a way to induce the size-quantization effect proposed by Hicks and Dresselhaus [18,19]. Hicks and Dresselhaus theoretically predicted that the size-quantization effect in a low-dimensional system can induce a sharp increase in the local density of states, which in turn can be utilized to enhance S of thermoelectric materials. The concept was experimentally demonstrated by Heremans *et al.* [20] on Bi nanowires embedded in porous host materials, for which S increased orders of magnitude due to the size-quantization effect. Unfortunately, at the time those results were produced, it proved impossible to insert a large enough volume fraction of Bi in the host material, so that the increase in electrical resistivity due to size quantization was not overcome by a corresponding decrease in thermal conductivity, as the overall thermal conductance was dominated by the porous host material [21].

Here we investigate the effect of nanostructuring in $Bi_{100-x}Sb_x$ alloys by synthesizing $Bi_{100-x}Sb_x/Al_2O_3$ nanocomposites ($x = 12$ and 18 at.%). By utilizing the ball-milling technique, we were able to synthesize bulk nanocomposite samples, thus avoiding the fill fraction issue in the previous study [20]. We introduced Al_2O_3 nanoparticles (diameter = 40 to 50 nm) with varying volume percentages in $Bi_{100-x}Sb_x$ host matrices, effectively creating nanocomposites with well-dispersed nanoscale inclusions. We present experimental results of thermal and electrical transport in the $Bi_{100-x}Sb_x/Al_2O_3$ samples, and show that zT reaches near 0.4 at 240 K. We discuss the results with regard to carrier scattering and carrier concentration, based on rigorous galvano- and thermomagnetic analyses.

II. EXPERIMENT

A. Sample preparation

The appropriate amounts of 6N-pure Alfa-Aesar Bi and Sb were coarsely ground with mortar and pestle in a glove box, and introduced into a stainless-steel ball-milling vessel. The appropriate amount of Alfa-Aesar NanoTek Al_2O_3 powder, with 40–50-nm-diameter particles, was added to the vessel. The vessel was sealed within a glove box, extracted from it, and the content was milled for 80 min in a SPEX 8000M high-energy ball mill. Materials were mixed and ground in stainless-steel vials with two $\frac{1}{2}$-in. and four $\frac{1}{4}$-in. stainless-steel balls. After this, the vessel was reintroduced into the glove box, and opened, and the powder was transferred into a graphite die. The powder was pressed using a 3-ton hydraulic press. The pressed pellets were introduced into a quartz ampoule, which was evacuated and sealed at less than 10^{-6} Torr, and the material was subsequently sintered at 265 °C for 150 h. The mass density of the samples was measured using the Archimedes method. All of the nanocomposite samples with Al_2O_3 show the quite consistent mass density of ~92% relative to their theoretical values, while the samples without Al_2O_3 have ~93%. Samples were then cut into approximately $2 \times 1 \times 7\,mm^3$ parallelepipeds, and their thermoelectric, thermomagnetic, and galvanomagnetic properties were measured at temperatures from 80 to 420 K and with magnetic field up to 1.4 T using a custom liquid nitrogen cryostat system.

Scanning electron microscopy (SEM) pictures for the $Bi_{82}Sb_{18}/Al_2O_3$ nanocomposite samples with 5 and 20 vol % Al_2O_3 nanoparticles are shown in Fig. 2. While fairly well distributed Al_2O_3 nanoparticles are observed, it is not clear

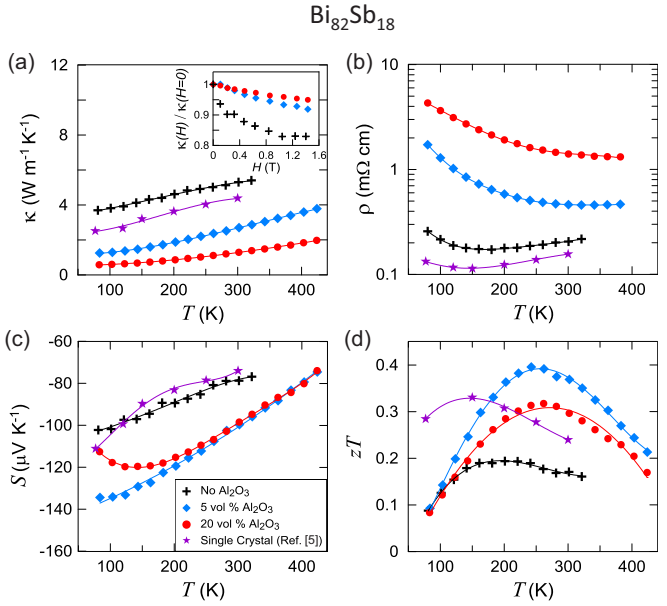

FIG. 3. Temperature dependence of thermoelectric properties of $Bi_{82}Sb_{18}$ alloy samples. (a) Thermal conductivity (κ); (b) electrical resistivity (ρ); (c) Seebeck coefficient (S); (d) figure of merit (zT). The data for the single-crystalline sample were calculated by taking a weighted average of the data from Ref. [5] along the three crystallographic directions. Inset in (a) shows the magnetic field dependence of κ normalized by the zero-field value at $T = 100$ K. Figure legend is included in (c). Symbols are experimental data points and lines are added to guide the eye.

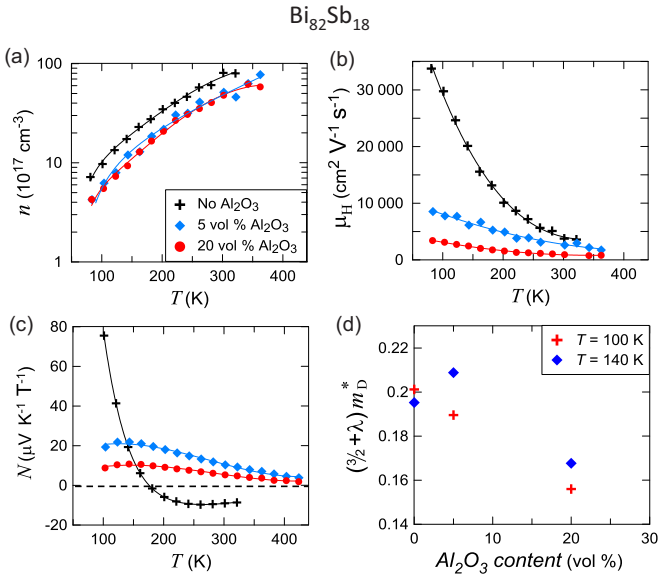

FIG. 4. Temperature dependence of (a) carrier concentration (n), (b) Hall mobility (μ_H), and (c) Nernst coefficient (N) of $Bi_{82}Sb_{18}$ alloy samples. Figure legend is included in (a). (d) Dependence of $(3/2 + \lambda)m^*$ on Al_2O_3 concentration at $T = 100$ and 140 K, where λ is the scattering parameter and m^* is the density-of-state effective mass of electrons. Symbols are experimental data points and lines are added to guide the eye.

whether effective nanoscale channels are formed in the samples. Seemingly, 5 vol % of Al_2O_3 is too scarce to form such channels.

B. $Bi_{82}Sb_{18}/Al_2O_3$ nanocomposites

Figure 3 shows the thermoelectric properties of $Bi_{82}Sb_{18}/Al_2O_3$ nanocomposite samples with 0, 5, and 20 vol % Al_2O_3. We compare the data to calculated values for the thermoelectric properties of the single-crystalline $Bi_{82}Sb_{18}$ sample in Ref. [5], by taking a weighted average of the data along the three crystallographic directions. $\kappa(T)$ of the nanocomposite samples shown in Fig. 3(a) is significantly reduced compared to that of the single-crystalline sample and decreases as the volume percentage of Al_2O_3 increases. It is possible to estimate how much reduction in $\kappa(T)$ comes from each of the electronic and lattice contributions by measuring the magnetic field dependence of the thermal conductivity, $\kappa(H)$, where H is the external magnetic field applied in the transverse direction. The inset in Fig. 3(a) shows $\kappa(H)$ normalized by the zero-field value, $\kappa(H)/\kappa(H = 0)$ at $T = 100$ K. The $\kappa(H)/\kappa(H = 0)$ of the $Bi_{82}Sb_{18}$/no Al_2O_3 sample decreases with increasing H, and saturates at $H > 1.0$ T. This saturation indicates complete suppression of the electronic contribution to κ, leaving only the lattice contribution [22,23]. The electronic contribution in the $Bi_{82}Sb_{18}$/no Al_2O_3 is estimated to be 17% of the total κ. By repeating the same procedure for the two $Bi_{82}Sb_{18}$ nanocomposite samples, we obtain the electronic contribution of 8% and 5% for the 5 and 20 vol % Al_2O_3 samples, respectively. The difference in those values between the no Al_2O_3 sample and the nanocomposite samples accounts for the amount of reduction in the electronic contribution due to the presence of Al_2O_3 nanoparticles—9% and 12% for the 5 and 20 vol % Al_2O_3 samples, respectively. The remaining 91% and 88% reductions come from the lattice contribution. Therefore, the reduction in $\kappa(T)$ in the $Bi_{82}Sb_{18}/Al_2O_3$ samples is mainly attributed to the reduction of the lattice thermal conductivity due to phonon scattering by the Al_2O_3 nanoparticles and grain boundaries in the polycrystalline samples. On the other hand, the electrical resistivity ($\rho = 1/\sigma$) shown in Fig. 3(b) shows a large increase over the measurement temperature regime as the Al_2O_3 content increases. The carrier concentration (n) data obtained from Hall coefficient (R_H) measurements, shown in Fig. 4(a), show that the addition of the Al_2O_3 slightly reduces n, but not so much as to account for the increase in $\rho(T)$. The Hall mobility (μ_H) data, shown in Fig. 4(b), suggest that the Al_2O_3 nanoparticles also strongly scatter conduction electrons. The ratios of the $\rho(T)$ of the materials for Al_2O_3 loadings of 0, 5, and 20 vol % are 1:3:9 at 300 K. The thermal resistivity, the inverse of the κ, increases in ratios of 1:2:6 at the same temperature. We conclude that the Al_2O_3 nanoparticles scatter electrons more than they scatter phonons, and that the ratio between the electrical and thermal conductivities is thus slightly unfavorable to zT. Sharp and Goldsmid theoretically studied the effect of grain boundary scattering on zT of SiGe, Bi-Sb, and Bi_2Te_3 alloys [24–26]. They concluded that while grain boundary scattering can significantly enhance the zT of SiGe alloys down to a certain grain size, it is unlikely to be useful for Bi-Sb and

Bi_2Te_3 alloys wherein conduction electrons with long mean free paths are scattered much more than phonons by small grain boundaries. Their prediction is consistent with what we observe in the $Bi_{82}Sb_{18}/Al_2O_3$ nanocomposite samples.

In contrast, $S(T)$ is very favorably influenced by the presence of Al_2O_3 nanoparticles [Fig. 3(c)]. The concentration of those particles has little effect, but their presence increases the absolute value of $S(T)$ by 25% near room temperature. This increase more than compensates the loss mentioned in the previous paragraph, so that the zT of the $Bi_{82}Sb_{18}/5\%Al_2O_3$ sample is improved above 180 K compared to that of the sample with no Al_2O_3 and reaches its maximum value ~0.4 at 240 K as shown in Fig. 3(d). It also is noted that the peak zT is shifted to higher temperatures for the nanocomposite samples. Since the origin of the improvement lies in the enhanced $S(T)$, we can speculate about the physical mechanisms that can give rise to the effect. The first possibility is the size-quantization effect in some channels of $Bi_{82}Sb_{18}$ alloys that might exist in between the Al_2O_3 nanoparticles. We exclude this possibility based on the SEM results (Fig. 2) as well as on the fact that no noticeable increase in the electron effective mass has been observed in the nanocomposite samples as described below.

A second possibility is an increase in the energy dependence of the relaxation time. Such a mechanism was proven to be the physical origin of a similar observation made in nanostructured PbTe [14] prepared in a similar way. Here as well, we explore such possibility by analyzing the thermomagnetic and galvanomagnetic properties. The magnetic field dependence of the Nernst voltage (not shown) becomes very nonlinear above 120 K, and shows the opposite sign between the low field ($\mu H \ll 1$, where μ is the electron mobility and H is the applied magnetic field) and the high field ($\mu H > 1$). Here we only consider the low-field ($\mu H \ll 1$) Nernst coefficient (N) in our analysis where the Nernst voltage is linear in H. The temperature dependence of the low-field N [Fig. 4(c)] shows a sharp contrast in its behavior between the samples with and without Al_2O_3 nanoparticles, indicating that different scattering mechanisms dominate in the two systems. While the low-field N of the samples with Al_2O_3 nanoparticles stays positive and is relatively small in the measured temperature range, that of the sample with no Al_2O_3 shows a sign change from negative to positive below 180 K where it also features a strong temperature dependence; this is normal, since the N is particularly sensitive to the details of the scattering mechanism. The scattering mechanism changes enough with the introduction of Al_2O_3 nanoparticles to affect the N, but not, as reported below, the S. Next, the "method of the four coefficients" [14,27] was applied to the $Bi_{82}Sb_{18}$ data. In this method, one uses four transport coefficients, the resistivity ($\rho = 1/\sigma$), Hall coefficient (R_H), Nernst coefficient (N), and thermopower (S), to determine four transport parameters, the density-of-states effective mass (m_D^*), Fermi energy (E_F), mobility (μ), and scattering parameter (λ). For nonparabolic and nondegenerate systems, the energy dependence of electron scattering is represented by that of the relaxation time as [27,28]

$$\tau = \tau_0 \frac{\gamma(E)^\lambda}{\gamma'(E)}, \tag{1}$$

where τ_0 is an energy-independent scaling coefficient, $\gamma(E) = E(1 + \frac{E}{E_g})$ (E_g is the energy band gap), γ' is the derivative of γ with respect to E, and λ is the scattering parameter whose value depends on the scattering mechanism. Typically, for acoustic phonon scattering, $\lambda = -0.5$ while for ionized impurity scattering, $\lambda = 1.5$, but in practice, given the error bars, one usually finds $-0.8 < \lambda < 1.6$. The electrical conductivity is [27]

$$\sigma = \frac{(2m_D^* k_B T)^{3/2}}{3\pi^2\hbar^3} \frac{e^2}{m_\alpha^*} \int_0^\infty \frac{\gamma(z)^{3/2}}{\gamma'(z)} \tau(z) \left(-\frac{\partial f_0}{\partial z}\right) dz \tag{2}$$

where e is the carrier charge; k_B is the Boltzmann constant; $\hbar$ is the reduced Planck constant; m_α^* is the effective mass along the crystallographic direction of the sample studied, or the appropriate average mass for polycrystals; and f_0 is the Fermi-Dirac distribution function. The low-field ($\mu H \ll 1$) Hall coefficient is

$$R_H = \frac{3K(K+2)}{(2K+1)^2} \frac{1}{ne} \frac{\left\{\int_0^\infty \frac{\gamma(z)^{3/2}}{[\gamma'(z)]^2} \tau^2(z) \left(-\frac{\partial f_0}{\partial z}\right) dz\right\} \left\{\int_0^\infty \gamma(z)^{3/2} \left(-\frac{\partial f_0}{\partial z}\right) dz\right\}}{\left\{\int_0^\infty \frac{\gamma(z)^{3/2}}{\gamma'(z)} \tau(z) \left(-\frac{\partial f_0}{\partial z}\right) dz\right\}^2}, \tag{3}$$

where K is the effective mass anisotropy coefficient; $K = m_l^*/m_t^*$ (m_l^* and m_t^* are the electron effective masses along the longitudinal and transverse directions, respectively). The low-field ($\mu H \ll 1$) isothermal Nernst coefficient is

$$N = R_H \sigma \frac{k_B}{e} \left\{ \frac{\int_0^\infty \frac{\gamma(z)^{3/2}}{[\gamma'(z)]^2} z\tau^2(z) \left(-\frac{\partial f_0}{\partial z}\right) dz}{\int_0^\infty \frac{\gamma(z)^{3/2}}{[\gamma'(z)]^2} \tau^2(z) \left(-\frac{\partial f_0}{\partial z}\right) dz} - \frac{\int_0^\infty \frac{\gamma(z)^{3/2}}{\gamma'(z)} z\tau(z) \left(-\frac{\partial f_0}{\partial z}\right) dz}{\int_0^\infty \frac{\gamma(z)^{3/2}}{\gamma'(z)} \tau(z) \left(-\frac{\partial f_0}{\partial z}\right) dz} \right\}, \tag{4}$$

and the thermopower is

$$S = \frac{k_B}{e} \left\{ \frac{\int_0^\infty \frac{\gamma(z)^{3/2}}{\gamma'(z)} z\tau(z) \left(-\frac{\partial f_0}{\partial z}\right) dz}{\int_0^\infty \frac{\gamma(z)^{3/2}}{\gamma'(z)} \tau(z) \left(-\frac{\partial f_0}{\partial z}\right) dz} - \frac{E_F}{k_B T} \right\}. \tag{5}$$

For a degenerate semiconductor ($E_F \gg k_B T$) with a parabolic band and a single type of carrier, the energy dependence of relaxation time is simplified as $\tau(E) \propto E^{\lambda}$, and Eqs. (2)–(5) are now written as [28]

$$\sigma = ne\mu, \tag{6}$$

$$R_H = \frac{1}{ne}, \tag{7}$$

$$N = \frac{\pi^2}{3}\left(\frac{k_B}{e}\right)\frac{k_B T}{E_F}\lambda\mu, \tag{8}$$

$$S = \frac{2\pi^{2/3}}{3^{5/3}}\frac{k_B^2}{e\hbar^2}T\left(\frac{3}{2}+\lambda\right)\frac{m_D^*}{n^{2/3}}. \tag{9}$$

As outlined above, Eqs. (6)–(9) are solved at each temperature for four transport parameters, m_D^*, E_F, μ, and λ. By using the m_D^* and λ derived from the method of the four coefficients and the n derived from the Hall measurements, we can find the origin of enhancement of S in the $Bi_{82}Sb_{18}/Al_2O_3$ nanocomposite samples. Figure 4(d) shows that $(3/2+\lambda)m_D^*$ does not have strong dependence either on the Al_2O_3 content or on temperature; all of the data points are scattered within (0.18 ± 0.03). This observation suggests that the enhanced S of the nanocomposite samples actually originates from their lower n, not from either increased m_D^* or λ. Jandl and Birkholz [7] also showed that slight p-type doping by tin could increase the n-type S value in $Bi_{95}Sb_5$ single crystals, thus leading to enhanced zT values above 200 K, which is consistent with our observation. Thus, we suggest that the lower S of both the sample with no Al_2O_3 and the single-crystalline sample from Ref. [5] is due to less optimally doped samples with larger n. Defects are known to alter the carrier concentration in Bi [29], so that it is likely that the presence of Al_2O_3 nanoparticles affects it as well. Vecchi *et al.* [30] reported the temperature dependence of the band gap between the conduction and valence bands at the L point for $Bi_{100-x}Sb_x$ ($0 \leqslant x \leqslant 15$) alloys, and showed that the band gap closes and band inversion happens near 180 K. Since we use the model for degenerate semiconductors based on a single type of carrier, we limit our analysis to the temperature range below 140 K where the thermal excitation is relatively less significant. It is also noted that the L-point conduction band in Bi-Sb alloys is known to be nonparabolic. While this nonparabolicity could also introduce errors in estimating the values of the transport parameters, we find that the temperature-independent trend of $(3/2+\lambda)m_D^*$ remains consistent.

C. $Bi_{88}Sb_{12}/Al_2O_3$ nanocomposites

The thermoelectric properties of $Bi_{88}Sb_{12}/Al_2O_3$ nanocomposite samples with 0, 5, 20, and 40 vol % Al_2O_3 are shown in Fig. 5, compared with those of a single-crystalline $Bi_{88}Sb_{12}$ sample calculated using the data from Ref. [5]. $\kappa(T)$ of the polycrystalline $Bi_{88}Sb_{12}$ sample is slightly lower than that of the single-crystalline sample, possibly due to its lower density as well as additional phonon scattering by grain boundary and defects. Introducing Al_2O_3 nanoparticles significantly reduces $\kappa(T)$, suggesting that the 40–50-nm nanoparticles effectively scatter phonons. $\rho(T)$ of the

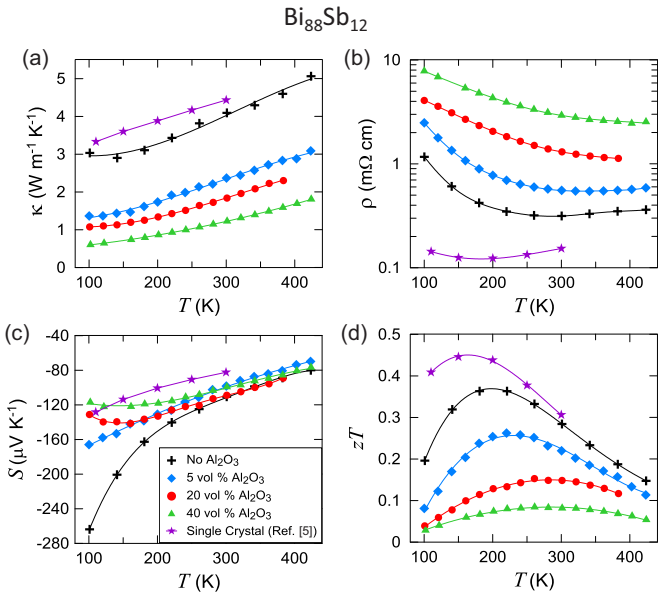

FIG. 5. Temperature dependence of thermoelectric properties of $Bi_{88}Sb_{12}$ alloy samples. (a) Thermal conductivity (κ); (b) electrical resistivity (ρ); (c) Seebeck coefficient (S); (d) figure of merit (zT). The data for the single-crystalline sample were calculated by taking a weighted average of the data from Ref. [5] along the three crystallographic directions. Figure legend is included in (c). Symbols are experimental data points and lines are added to guide the eye.

polycrystalline samples is considerably higher than that of the single-crystalline samples, and rapidly increases as the Al_2O_3 content increases. It is noted that the difference in $\rho(T)$ between the polycrystalline $Bi_{88}Sb_{12}$ sample and the single-crystalline sample is larger than that in $\kappa(T)$ between the two samples. Additionally, the rate at which $\rho(T)$ increases with increasing Al_2O_3 content is much larger than the rate at which $\kappa(T)$ decreases. Figure 6(b) confirms that one of the mechanisms at work to increase $\rho(T)$ is indeed scattering of conduction electrons by Al_2O_3 nanoparticles. This conclusion is in line with the case of $Bi_{82}Sb_{18}/Al_2O_3$ nanocomposite samples. The consistent results from the two different sample sets indicate that the Al_2O_3 nanoparticles, small grain boundaries, and defects in the $Bi_{100-x}Sb_x$ polycrystalline samples scatter phonons and electrons simultaneously, with more effect on the latter, thus unfavorably affecting zT values.

$S(T)$ of the polycrystalline samples shows enhancement compared to that of the single crystal, consistent with the case of $Bi_{82}Sb_{18}$ samples. The behavior around and below 100 K of the polycrystalline $Bi_{88}Sb_{12}$ sample containing no Al_2O_3 is indicative of a classical narrow-gap semiconductor which shows carrier freeze-out. All samples containing Al_2O_3 have a similar $S(T)$, but their curves never reach the high $S(T)$ value of the polycrystalline $Bi_{88}Sb_{12}$ sample with no Al_2O_3 at 100 K. Overall, zT of the polycrystalline $Bi_{88}Sb_{12}$ samples is inferior to that of the single-crystalline sample over the measured temperature range, contrary to the case of $Bi_{82}Sb_{18}$ samples. This is again due to the significantly reduced σ/κ ratio, which in this case is not compensated by the amount of increase in $S(T)$. Introducing Al_2O_3 nanoparticles further

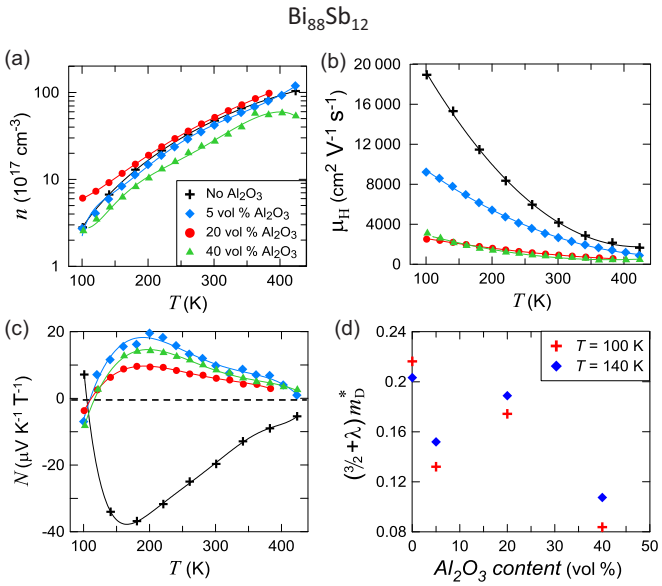

FIG. 6. Temperature dependence of (a) carrier concentration (n), (b) Hall mobility (μ_H), and (c) Nernst coefficient (N) of $Bi_{88}Sb_{12}$ alloy samples. Figure legend is included in (a). (d) Dependence of $(3/2+\lambda)m^*$ on Al_2O_3 concentration at $T = 100$ and 140 K, where λ is the scattering parameter and m^* is the density-of-state effective mass of electrons. Symbols are experimental data points and lines are added to guide the eye.

reduces zT in the $Bi_{88}Sb_{12}/Al_2O_3$ samples, because the presence of the Al_2O_3 nanoparticles further deteriorates the σ/κ ratio while it affects $S(T)$ little. This result is also in contrast to that of the $Bi_{82}Sb_{18}/Al_2O_3$ samples, where the samples with Al_2O_3 nanoparticles show better zT above 180 K. The discrepancy between the two systems is mainly attributed to the degree of optimal doping of the samples. While the $Bi_{88}Sb_{12}/Al_2O_3$ samples also exhibit weak dependence of $(3/2+\lambda)m^*_D$ on the Al_2O_3 content [Fig. 6(d)], there is almost no difference in n between the samples with and without Al_2O_3 nanoparticles [Fig. 6(a)]. Combined together, this leads to the fairly consistent $S(T)$ between those samples, thus making their zT dependent mostly on the σ/κ ratio. As we have discussed earlier, the $Bi_{82}Sb_{18}/Al_2O_3$ samples, on the other hand, have quite different n between the samples with and without Al_2O_3 nanoparticles: The samples with Al_2O_3 nanoparticles have smaller n, which yields the improved zT above 180 K compared to the sample without the nanoparticles. Therefore, we can conclude that in $Bi_{100-x}Sb_x$ alloys ($x = 12$ and 18 at.%), introduction of nanoscale inclusions unfavorably affects the σ/κ ratio as predicted by Sharp and Goldsmid [24–26], while it barely affects S through altering the value of $(3/2+\lambda)m^*_D$. It is noted, nevertheless, that the zT of the nanocomposite samples can still be improved over that of the single-crystalline sample by carefully adjusting n and thus enhancing S as in the case of $Bi_{82}Sb_{18}/Al_2O_3$ samples.

III. CONCLUSIONS

In summary, we present the experimental study of thermoelectric properties of $Bi_{100-x}Sb_x/Al_2O_3$ nanocomposites ($x = 12$ and 18 at.%), wherein we intentionally introduced various volume percentages of Al_2O_3 nanoparticles with a goal of creating nanoscale channels in the $Bi_{100-x}Sb_x$ matrix that could possibly increase the Seebeck coefficient either by size-quantization effects or by enhanced scattering parameter. No proof was found of either effect in this study. The Al_2O_3 nanoparticles may scatter phonons leading to the reduction of the lattice thermal conductivity. While such reduction of the lattice thermal conductivity is experimentally confirmed, it is found that the Al_2O_3 nanoparticles also strongly scatter conduction electrons, resulting in unfavorable net effect on the electrical to thermal conductivity ratio. On the other hand, the enhancement of the Seebeck coefficient in the $Bi_{82}Sb_{18}/Al_2O_3$ nanocomposite samples is large enough to compensate the loss due to scattering of conduction electrons, which overall leads to an improved figure of merit above 180 K compared to that of a single-crystalline counterpart as well as the sample with no Al_2O_3. The peak figure of merit is shifted to higher temperatures for the nanocomposite samples, reaching the value of ~0.4 at 240 K. Detailed galvano- and thermomagnetic studies reveal that the enhanced Seebeck coefficient of the $Bi_{82}Sb_{18}/Al_2O_3$ nanocomposite samples is originated from a more optimal doping level of the samples. In contrast, the presence of the Al_2O_3 nanoparticles hardly affects the effective mass or the scattering parameter. Our study suggests the possibility of improving thermoelectric performance of nanocomposites by optimal doping, even for materials wherein the presence of nanostructure yields an unfavorable effect on the electrical to thermal conductivity ratio.

ACKNOWLEDGMENTS

The work was supported by the Basic Science Research Program through the National Research Foundation of Korea (NRF) funded by the Ministry of Education (NRF-2017R1D1A1B03034331), and by the Nano Material Technology Development Program through the NRF funded by the Ministry of Science and ICT (NRF-2017M3A7B8065589). J.P.H. is supported by the Center for Emergent Materials: an NSF MRSEC under Award No. DMR-1420451.

[1] J. P. Heremans and H. Jin, Thermoelectric and spin-caloritronic coolers: from basics to recent developments, Proc. SPIE **9765**, 976507 (2016).

[2] C. F. Gallo, B. S. Chandrasekhar, and P. H. Sutter, Transport properties of bismuth single crystals, J. Appl. Phys. **34**, 144 (1963).

[3] H. Jin, C. M. Joworski, and J. P. Heremans, Enhancement in the figure of merit of p-type $Bi_{100-x}Sb_x$ alloys through multiple valence-band doping, Appl. Phys. Lett. **101**, 053904 (2012).

[4] J. P. Heremans, R. J. Cava, and N. Samarth, Tetradymites as thermoelectrics and topological insulators, Nat. Rev. Mater. **2**, 17049 (2017).

[5] W. M. Yim and A. Amith, Bi-Sb alloys for magneto-thermoelectric and thermomagnetic cooling, Solid-State Electron. **15**, 1141 (1972).

[6] G. E. Smith and R. Wolfe, Thermoelectric properties of bismuth-antimony alloys, J. Appl. Phys. **33**, 841 (1962).

[7] P. Jandl and U. Birkholz, Thermogalvanomagnetic properties of Sn-doped $Bi_{95}Sb_5$ and its application for solid state cooling, J. Appl. Phys. **76**, 7351 (1994).

[8] V. S. Zemskov, A. D. Belaya, U. S. Beluy, and G. N. Kozhemyakin, Growth and investigation of thermoelectric properties of Bi-Sb alloy single crystals, J. Cryst. Growth **212**, 161 (2000).

[9] N. A. Sidorenko and L. D. Ivanova, Bi-Sb solid solutions: Potential materials for high-efficiency thermoelectric cooling to below 180 K, Inorg. Mater. **37**, 331 (2001).

[10] B. Lenoir, M. Cassart, J.-P. Michenaud, H. Scherrer, and S. Scherrer, Transport properties of Bi-rich Bi-Sb alloys, J. Phys. Chem. Solids **57**, 89 (1996).

[11] B. Lenoir, A. Dauscher, M. Cassart, Yu. I. Ravich, and H. Scherrer, Effect of antimony content on the thermoelectric figure of merit of $Bi_{1-x}Sb_x$ alloys, J. Phys. Chem. Solids **59**, 129 (1998).

[12] R. Martin-Lopez, A. Dauscher, H. Scherrer, J. Hejtmanek, H. Kenzari, and B. Lenoir, Thermoelectric properties of mechanically alloyed Bi-Sb alloys, Appl. Phys. A **68**, 597 (1999).

[13] X. Devaux, F. Brochin, R. Martin-Lopez, and H. Scherrer, Study of the microstructure influence on the transport properties of $Bi_{86.5}Sb_{13.5}$ polycrystalline alloy, J. Phys. Chem. Solids **63**, 119 (2002).

[14] J. P. Heremans, C. M. Thrush, and D. T. Morelli, Thermopower enhancement in lead telluride nanostructures, Phys. Rev. B **70**, 115334 (2004).

[15] B. Poudel, Q. Hao, Y. Ma, Y. Lan, A. Minnich, B. Yu, X. Yan, D. Wang, A. Muto, D. Vashaee, X. Chen, J. Liu, M. S. Dresselhaus, G. Chen, and Z. Ren, High-thermoelectric performance of nanostructured bismuth antimony telluride bulk alloys, Science **320**, 634 (2008).

[16] T. Zhu, C. Fu, H. Xie, Y. Liu, and X. Zhao, High efficiency half-Heusler thermoelectric materials for energy harvesting, Adv. Energy Mater. **5**, 1500588 (2015).

[17] W. Xie, A. Weidenkaff, X. Tang, Q. Zhang, J. Poon, and T. M. Tritt, Recent advances in nanostructured thermoelectric half-Heusler compounds, Nanomaterials **2**, 379 (2012).

[18] L. D. Hicks and M. S. Dresselhaus, Effect of quantum-well structures on the thermoelectric figure of merit, Phys. Rev. B **47**, 12727 (1993).

[19] L. D. Hicks and M. S. Dresselhaus, Thermoelectric figure of merit of a one-dimensional conductor, Phys. Rev. B **47**, 16631 (1993).

[20] J. P. Heremans, C. M. Thrush, D. T. Morelli, and M-C. Wu, Thermoelectric Power of Bismuth Nanocomposites, Phys. Rev. Lett. **88**, 216801 (2002).

[21] J. P. Heremans, Low-dimensional thermoelectricity, Acta Phys. Pol. **108**, 609 (2005).

[22] J.-P. Issi, J. P. Heremans, and M. S. Dresselhaus, Electronic and lattice contributions to the thermal conductivity of graphite intercalation compounds, Phys. Rev. B **27**, 1333 (1983).

[23] C. Uher and H. J. Goldsmid, Separation of the electronic and lattice thermal conductivities in bismuth crystals, Phys. Status Solidi B **65**, 765 (1974).

[24] J. W. Sharp and H. J. Goldsmid, Boundary scattering of charge carriers and phonons, in *Proceedings of the 18th International Conference on Thermoelectrics* (IEEE, Baltimore, MD, 1999), p. 709.

[25] E. H. Volckmann, H. J. Goldsmid, and J. Sharp, Observation of the effect of grain size on the lattice thermal conductivity of polycrystalline bismuth antimony, in *Proceedings of the 15th International Conference on Thermoelectrics* (IEEE, Pasadena, CA, 1996), p. 22.

[26] J. W. Sharp, E. H. Volckmann, and H. J. Goldsmid, The thermal conductivity of polycrystalline $Bi_{88}Sb_{12}$, Phys. Status Solidi A **185**, 257 (2001).

[27] J. P. Heremans, C. M. Thrush, and D. T. Morelli, Thermopower enhancement in PbTe with Pb precipitates, J. Appl. Phys. **98**, 063703 (2005).

[28] Yu. I. Ravich, B. A. Efimova, and I. A. Smirnov, *Semiconducting Lead Chalcogenides* (Plenum, New York, 1970).

[29] M. Le Goff and J. P. Heremans, Galvanomagnetic properties at 4.2 K of bismuth irradiated with fast electrons, J. Phys. F: Met. Phys. **14**, 399 (1984).

[30] M. P. Vecchi, E. Mendez, and M. S. Dresselhaus, Temperature dependence of the band parameters in Bi and $Bi_{1-x}Sb_x$ alloys, in *Proceedings of the 13th International Conference on Physics of Semiconductors* (Rome, Italy, 1976), p. 459.